

Autonomous Scanning for Endoscopic Mosaicing and 3D Fusion

Lin Zhang, Menglong Ye, Petros Giataganas, Michael Hughes and Guang-Zhong Yang

Abstract—Robotic-assisted Minimally Invasive Surgery (RMIS) can benefit from the automation of common, repetitive or well-defined but ergonomically difficult tasks. One such task is the scanning of a pick-up endoscopy probe over a complex, undulating tissue surface in order to enhance the effective field-of-view through video mosaicing. In this paper, the da Vinci[®] surgical robot, through the dVRK framework, is used for autonomous scanning and 2D mosaicing over a user-defined region of interest. To achieve the level of precision required for high quality large-area mosaic generation, which relies on sufficient overlap between consecutive image frames, visual servoing is performed using a tracking marker attached to the probe. The resulting sub-millimetre accuracy of the probe motion allows for the generation of large endoscopy mosaics with minimal intervention from the surgeon. It also allows the probe to be maintained in an orientation perpendicular to the local tissue surface, providing optimal imaging results. Images are streamed from the endoscope and overlaid live onto the surgeons view, while 2D mosaics are generated in real-time, and fused into a 3D stereo reconstruction of the surgical scene, thus providing intuitive visualisation and fusion of the multi-scale images. The system therefore offers significant potential to enhance surgical procedures, by providing the operator with cellular-scale information over a larger area than could typically be achieved by manual scanning.

I. INTRODUCTION

Minimally Invasive Surgery (MIS), in which surgical procedures are performed through small incisions, is a widely used and effective approach for oncological treatments. It has significant advantages over the traditional open techniques, in terms of reduced blood loss and postoperative pain, lower infection rates, and shorter hospital stays. However, MIS has some drawbacks, which include the constrained motion due to ‘keyhole’ access, poor depth perception from only a monocular laparoscope, and lack of direct tissue interaction. To provide better manipulation and depth perception, robotic systems with stereo vision have been developed for MIS. In particular, the da Vinci[®] robot (Intuitive Surgical Inc., CA) is a successful surgical platform which has been widely used in the treatment of gynecological and urological cancer. However, the da Vinci[®] robot is purely a master-slave system that only provides tele-operation abilities to the surgeons, with no automation or artificial intelligence features.

Whilst human guidance is essential for MIS, a recent review [1] has concluded that surgical automation can be used for some important steps of the operation, which can then reduce the cognitive load of the surgeon during certain surgical tasks that require repetitive and precise motion. To

this end, studies have been conducted, for instance, to maintain consistent motion for ultrasound elastography [2], or to automatically compensate the heart motion for cardiovascular surgery [3]. In [4], a human-machine collaborative framework was proposed to improve surgeons’ performance by semi-automating surgical subtasks. Further studies have also investigated how to perform automatic surgical debridement [5], tissue dissection [6], and brain ablation [7].

Another obvious target for automation is the process of generating *in situ* microscopic images of tissue using probe-based confocal laser endoscopy (pCLE), such that the microscopic images can be used for *in vivo* and *in situ* pathology analysis. Endoscopy has been used extensively for diagnostic and surgical procedures in the gastrointestinal tract and abdominal organs [8], [9], mainly to discriminate between normal and cancerous tissue regions. However, the miniaturisation requirement for the probe results in a limited field-of-view (FoV) of typically 0.25-1 mm, and therefore, it is difficult to characterise larger areas of tissue or to return to previously sampled points [10]. Furthermore, retrieving high quality and stable microscopic images with a manually manipulated probe is a challenging task, particularly when the operator attempts to ‘mosaic’ images to synthesise a larger FoV comparable to histological images. Mosaicing requires the operator to maintain optimal probe pose and tissue-contact while performing slow and controlled scanning motions with sub-millimetre accuracy [11].

Recent works have been proposed to combine robotised instruments with the endoscopy probe so as to achieve smooth and steady scanning, allowing consistent image mosaicing for real-time pathological analysis. These developments have included novel robotic mechanisms for 2D scanning [12]–[14] or for maintaining a desired probe-tissue contact force [11]. Integrations with existing robotic systems, such as the da Vinci[®] [15], [16], have also been investigated. However, with a weak depth perception and poor ergonomics, it is still difficult for clinicians to conduct a continuous and smooth microscopic scan during tele-operated surgery. Maintaining the probe in specific orientation and ensuring continuous contact with the surface remains a challenging and tedious task. Therefore, the development of an autonomous scanning system for endoscopy would benefit surgical operations by reducing the cognitive load on users and improving scanning accuracies over larger 3D surfaces.

In this work, we present a 6 degree-of-freedom (DoF) visual servoing method based on the da Vinci[®] robot with the da Vinci Research Kit (dVRK). With our proposed approach, the robot is able to achieve smooth motion with

All authors are with The Hamlyn Centre for Robotic Surgery, Institute of Global Health Innovation, Imperial College London, SW7 2AZ, London, UK

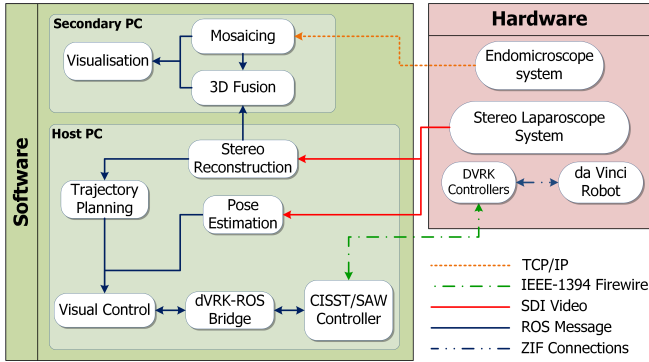


Fig. 1. An overview of our proposed system framework for autonomous endoscopic scanning and 3D mosaicing.

sub-millimetre accuracy, and we have demonstrated that an autonomous large-area endoscopy scan can be performed by the robot over a user-defined area. In addition, to facilitate intraoperative tissue diagnosis and identification, a 3D visualisation method is proposed to fuse the 3D tissue surface with microscopic mosaics on-the-fly, which is an improvement over the work of [17]. This 3D fusion approach is designed to provide the surgeon with an intuitive and effective real-time visualisation of multi-scale imaging information, which supports surgical diagnosis and planning. Our framework has been tested on phantom and *ex vivo* tissue experiments and the results have shown its clinical value.

II. METHODOLOGY

A. System Overview

The hardware components of the proposed framework, which is highlighted in red in Fig. 1, consist of a patient side manipulator (PSM) of a da Vinci[®] robot with dVRK controllers, a stereo laparoscope, and a custom endomicroscopy system. The dVRK controllers are connected to a host PC via a IEEE 1394 firewire interface in a daisy chain topology. The stereoscopic system provides SD (720x576) video streaming for both left and right channels at 25 Hz. In the host PC, the stereo stream is captured by a Kona 4 PCIe frame grabber (AJA Video System).

The endomicroscope system is an in-house laser line-scanning type system (which is under review elsewhere), modified from a previously published device [18], coupled to a Cellvizio UHD Probe (Mauna Kea Technologies). The probe, which consists of a 30,000 core fibre imaging bundle and a micro-lens, provides a FoV of 240 μm and a fibre-sampling limited resolution of approximately 2.4 μm . The line-scanning system provides optical sectioning, meaning that the endomicroscope collects light only from a in-focus plane approximately 20 μm in depth. The microscopic images are captured in 300x300 pixels, which are served to the the controller at 80 Hz via a TCP/IP connection. In addition to the host PC, we have used a second PC with modest configurations dedicated to perform 2D mosaicing and 3D visualisation.

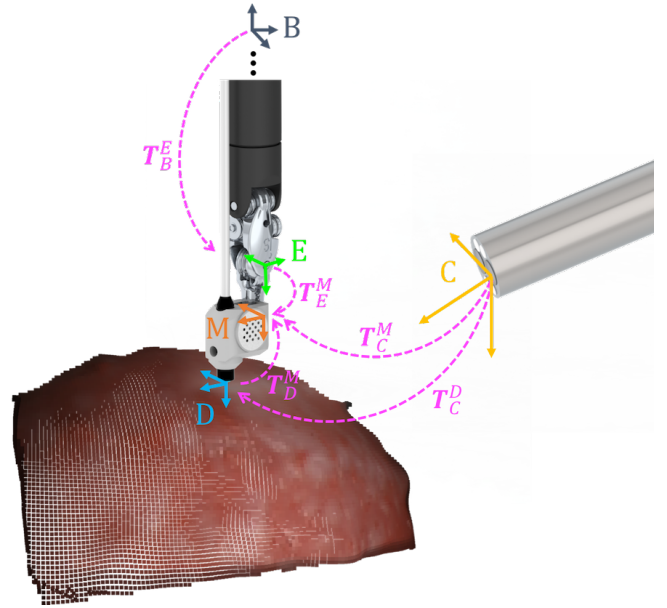


Fig. 2. A description of coordinate systems (frames) and related transformations. B : robot base frame; E : end-effector frame; M : marker frame; D : probe tip frame; C : camera frame.

The software component of the proposed framework is implemented based on the Robot Operating System (ROS) highlighted in green in Fig. 1. The stereo images captured from the camera are used for 3D tissue surface reconstruction via a stereo matching method. The reconstructed 3D surface is used for two purposes: (1) to plan a scanning trajectory based on its position and normal information; (2) to provide 3D fusion with the 2D image mosaics. The video stream from the laparoscope system is also used for pose estimation of the endomicroscopy probe.

As shown in Fig. 2, the end-effector of the robot grasps an adapter that holds the endomicroscopy probe. A marker (KeyDot[®], Key Surgical, Minnesota) is attached to the adapter for accurate pose estimation of the probe. The stereo system are calibrated using the method in [19] to obtain the intrinsic and extrinsic camera parameters, such that the 3D depths of the tissue can be recovered via stereo matching. The trajectory for an endomicroscopy scan can be planned with a simple 2D position input from the user who identifies the area-of-interest for tissue diagnosis.

A visual control component closes the loop by comparing the current and desired probe poses and commanding the robot to minimise their difference, which assists the probe to follow the planned trajectory. The robot's end-effector Cartesian pose is read and set via a dVRK-ROS component which is connected to a low level PID controller implemented by the SAW package using the cisst library [20]. Microscopic images captured from the endomicroscopy system are stitched together in real-time based on normalised cross-correlation. The image mosaic is fused with the reconstructed surface on-the-fly to provide both macro- and micro-views of the scanned region. With accurate and robust pose estimation,

our visual servoing approach enables the probe to conduct smooth and accurate scanning, so as to achieve continuous image mosaicing over a large and complex 3D surface intraoperatively.

B. Trajectory Planning Based on 3D Reconstruction

In this work, the scanning trajectory is planned to follow the 3D profile of the tissue surface. The Efficient LArge-scale Stereo (ELAS) [21] approach has been adopted for 3D surface reconstruction. The method starts the stereo matching from a set of sparse points. To achieve dense matching, these sparse points are then triangulated in 2D, such that the remaining points can be efficiently matched inside the triangles. To improve the surface smoothness (required for microscopic scanning), a box filter is applied on the disparity map, which aims to remove the outlier matches in poorly-textured areas. Furthermore, the stereo images are downsampled to 180x144 before stereo matching, enabling real-time performance.

Our trajectory planning can be started simply with a 2D position input (which can be initiated manually) on either of the stereo images. In the envisioned clinical scenario, this 2D point would represent the location of the area of interest for pathological analysis by endomicroscopy. As the probe has fixed position relative to the adapter, a rigid transformation can be found between the tip of the probe and the KeyDot[®] marker. For clarity, the definitions of the coordinate systems have been provided in Fig. 2. We denote C as the camera frame (coordinate system), and M and D as the marker frame and the tip frame of the probe, respectively. Let \mathbf{T}_C^M be the representation of the marker pose in the camera frame, and \mathbf{T}_C^D and \mathbf{T}_D^M be the transformations from the camera to the probe tip frame, and the probe tip frame to the marker frame, respectively. Therefore, we have

$$\mathbf{T}_C^M = \mathbf{T}_C^D \cdot \mathbf{T}_D^M \quad (1)$$

The scanning trajectory, which is a sequence of probe tip poses in the camera frame (\mathbf{T}_C^D), is planned in two stages: the global trajectory planning, which moves the probe to the starting pose for scanning, and the local trajectory planning, which performs high resolution scanning from the starting pose. To estimate the probe tip poses in the global trajectory, linear interpolation and spherical linear interpolation are used for translation and rotation, respectively. We have adopted a 2D raster pattern for the local trajectory, however, the same approach could be extended to other scanning patterns such as spirals. The local trajectory consists of a set of sparse 3D point locations forming the raster pattern. The desired orientation of the probe tip at each point is determined using the surface normals, so as to keep the probe tip perpendicular to the surface, a fact that is essential for high quality microscopic image retrieval.

As the endomicroscopy probe should be in direct contact with the tissue, changes of direction (moving between lines in the raster) result in tissue deformation and essentially loading and unloading of the tissue [22]. In order to minimise tissue deformation, we add an extra loading-unloading phase

between two scanning lines, where the probe advances further than the limit of the planned trajectory, as shown in Fig. 4(b). This also helps compensate for the backlash of the robot which occurs during large directional changes.

The sparse probe poses, including the loading-unloading phase, are then interpolated to a spacing comparable to the FoV of the endomicroscope. This trajectory is transformed from the probe tip to the marker frame, so that visual servoing control can be applied to assist scanning, using Equation 1, given the rigid transformation \mathbf{T}_C^M .

C. Visual Servoing with Real-time Pose Estimation

There are two common schemes for the camera system used in a robotic-control loop. One is referred to as eye-in-hand, where the camera is rigidly mounted on the end-effector, and the second is eye-to-hand, where the camera observes the robot in its workspace. In an eye-to-hand setting, which is used in this work, there are two rigid transformations that can be applied in order to transform the trajectory from the camera to the robot base frame: the robot-eye transformation between the robot base and camera, and the hand-tool transformation between the end-effector and the tool attached to it.

In our framework, we compute the hand-tool transformation between the end-effector and marker on the adaptor via a standard hand-eye calibration approach [23]. The advantage of using the hand-tool transformation is that it will not be affected when the robot and camera are repositioned. Therefore, hand-tool transformation is more practical during surgical procedures. Although the transformation would change slightly after the adapter is re-grasped, we found that a small error (a few millimetres) in the hand-tool transformation is tolerable for the visual servoing control, as long as the adapter is grasped in a similar way. In the presence of small errors in the hand-tool transformation, we propose to use a visual servoing approach for smooth and accurate microscopic scanning. The visual servoing approach includes two main steps: continuous and accurate probe pose estimation and relative commanding pose computation.

For probe pose estimation, a marker with asymmetric dots is attached to the adapter (see Fig. 2). In this work, we have used a vision-based detection-tracking method for marker recognition. The detection component is based on blob detection similar to [24], which is applied on every image in the sequence. In order to improve the marker recognition rate, we have included a tracking component based on pyramidal optical flow [25] to track the dots of the marker in time. Once the marker pattern is recognised in an image, the efficient perspective-n-points algorithm [26] is applied to calculate the marker pose based on 2D-3D correspondences. This detection-tracking method is efficient and runs in real-time at ~ 24 Hz in our host PC.

Given a current marker pose (from estimation) \mathbf{T}_C^{M*} and a desired pose \mathbf{T}_C^M in the camera frame (in the planned trajectory), a new command pose can be calculated for the robot to minimise the difference between them. The relative

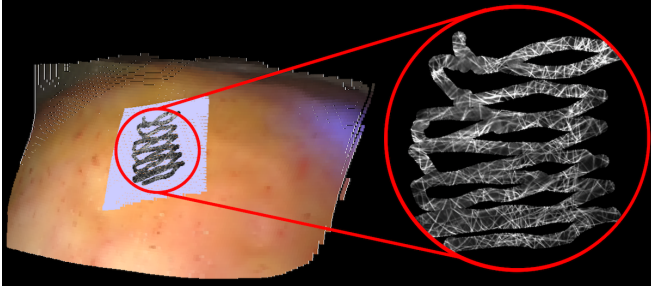


Fig. 3. 3D fusion. The surface is densely interpolated on the area (colored as gray) for pathology analysis, and 2D-3D mapping is created so that visualisation of mosaics on 3D can be updated efficiently.

marker pose denoted as $\mathbf{T}_{M^*}^M$ can be calculated as:

$$\mathbf{T}_{M^*}^M = \left(\mathbf{T}_C^M\right)^{-1} \cdot \mathbf{T}_C^M \quad (2)$$

Therefore, the relative end-effector pose is derived as:

$$\mathbf{T}_{E^*}^E = \left(\mathbf{T}_{M^*}^E\right)^{-1} \cdot \mathbf{T}_{M^*}^M \cdot \mathbf{T}_M^E \quad (3)$$

where \mathbf{T}_M^E is the hand-tool transformation between the marker and the PSM end-effector calibrated via a hand-eye calibration.

As mentioned, the visual servoing approach is able to compensate for the calibration error when deriving $\mathbf{T}_{M^*}^E$. This is because the relative poses of the end-effector $\mathbf{T}_{E^*}^E$ along the trajectory are computed with respect to the camera coordinate frame using only visual information. Therefore, correction commands are sent to the robot until the pose errors in the camera coordinate frame are minimised.

Finally, given the relative pose, the correction command is a desired end-effector pose in the robot base frame, which is calculated as:

$$\mathbf{T}_B^E = \mathbf{T}_B^{E^*} \cdot \mathbf{T}_{E^*}^E \quad (4)$$

The vision-based correction is performed on every pose along the planned trajectory. Furthermore, in order to produce smooth scanning motion, the trajectory between two adjacent poses is interpolated and executed using the robot kinematic model.

D. Endoscopic 3D Fusion and Visualisation

With the proposed 6-DoF visual servoing approach, the robot end-effector can adapt the pose of the mini-probe to the tissue surface. This enables us to achieve 3D fusion between macro- and micro-views, which are obtained from the stereo camera and the endomicroscope, respectively. For endomicroscopy image mosaicing, we have used an approach similar to standard real-time techniques in [18], [27], using normalised cross-correlation to estimate the relative shift between each pair of consecutive frames. To avoid overwriting information from previous frames and minimise the lighting effects in overlapping edges, image blending is applied on the mosaic image.

It should be noted that the image mosaics are generated in a 2D image space with much higher resolution than the

TABLE I
STEREO RECONSTRUCTION ACCURACY

		ELAS [21]	COCV [28]
Cardiac1	MAE (mm)	0.89 ± 0.70	1.24 ± 0.89
	RMS (mm)	1.31 ± 0.98	1.85 ± 0.82
Cardiac2	MAE (mm)	1.21 ± 1.56	1.47 ± 1.23
	RMS (mm)	1.77 ± 2.16	2.66 ± 1.47

3D tissue surface obtained from a standard stereoscope. To deal with the difference in resolutions, we have interpolated the 3D tissue surface to achieve the same resolution as the microscopic images. The interpolation is based on Radial Basis Functions (RBF), and can be performed immediately following stereo reconstruction. Efficient 2D-3D mapping can therefore be established for 3D fusion. The main steps of the 3D fusion process are: (1) 3D tissue surface reconstruction from stereo images; (2) Interpolation of the 3D surface to achieve microscopic resolution; (3) Creation of a 2D-3D mapping from the 2D pixels on the microscopic image mosaics to the interpolated 3D surface. (4) Update of the 3D surface on-the-fly when the microscopic images are being mosaicked. With a pre-interpolated 3D surface, the depth fusion task is efficient and can be performed at 25Hz, and to further improve the efficiency of the surface interpolation, it is only performed over the planned scan area. An illustration of the 3D fusion has been included in Fig. 3.

We provide three ways to visualise the scanning and mosaicing on-the-fly: (1) A view from the camera that observes the robot and target tissue; (2) A real-time updated 2D mosaicing map; (3) An online updating 3D fusion of microscopic images onto the reconstructed surface. To assist the users who desire to observe not only the scanning process but also the endomicroscopy image feed, we overlay the endomicroscopy images over the marker on the probe, in a form of augmented reality, as shown in Fig. 5(b) and (d).

III. EXPERIMENTS AND RESULTS

A. Stereo Validation

For assessing the accuracy of ELAS stereo reconstruction, we have provided a comparison of the method to the state-of-the-art [28] on the Hamlyn cardiac datasets (<http://hamlyn.doc.ic.ac.uk/vision/>). The results are provided in Table I, which have shown that the ELAS method provides competitive accuracies, while achieves real-time performance at 25Hz without any GPU programming.

B. Validation of Visual Servoing

To quantitatively validate the proposed visual servoing approach, we used the Optotrak Certus system (Northern Digital Inc, Canada) which can achieve 0.1 mm accuracy. Optical sensors were attached to a custom probe adapter, so that a rigid transformation could be found between the optical sensors and the marker frame. We ran ten trials for validation; the first five trials were for 2x2 mm scanning regions, while the other 5 trials used 3x3 mm regions. Each trial consisted of two runs that included trajectory-following

TABLE II
POSE ESTIMATION ERROR (MEAN \pm STD)

Trial	Local Translation Error (mm)		Overall Translation Error (mm)		Local Rotation Error (degrees)		Overall Rotation Error (degrees)	
	VS	KM	VS	KM	VS	KM	VS	KM
Trial 1	0.238 \pm 0.06	0.863 \pm 0.26	0.846 \pm 0.08	3.118 \pm 0.51	0.89 \pm 0.55	4.51 \pm 1.45	0.86 \pm 0.46	4.70 \pm 1.07
Trial 2	0.222 \pm 0.08	0.360 \pm 0.21	1.090 \pm 0.14	1.387 \pm 0.11	1.21 \pm 0.53	3.57 \pm 0.79	1.28 \pm 0.50	3.68 \pm 0.63
Trial 3	0.189 \pm 0.08	0.507 \pm 0.16	0.948 \pm 0.13	2.045 \pm 0.33	1.19 \pm 0.55	1.96 \pm 1.00	1.23 \pm 0.53	2.06 \pm 0.97
Trial 4	0.185 \pm 0.07	0.588 \pm 0.37	0.946 \pm 0.19	2.364 \pm 0.54	1.54 \pm 0.46	5.54 \pm 1.27	1.54 \pm 0.34	5.76 \pm 0.61
Trial 5	0.172 \pm 0.06	0.462 \pm 0.27	0.911 \pm 0.16	2.529 \pm 0.51	1.44 \pm 0.55	5.62 \pm 1.11	1.43 \pm 0.47	5.81 \pm 0.49
Trial 6	0.226 \pm 0.07	0.915 \pm 0.40	0.930 \pm 0.15	3.182 \pm 0.52	1.57 \pm 0.49	5.22 \pm 1.08	1.57 \pm 0.44	5.29 \pm 0.82
Trial 7	0.247 \pm 0.06	0.909 \pm 0.37	1.102 \pm 0.13	4.073 \pm 0.68	1.11 \pm 0.48	4.05 \pm 0.87	1.08 \pm 0.39	4.10 \pm 0.75
Trial 8	0.303 \pm 0.09	0.542 \pm 0.17	0.945 \pm 0.11	2.583 \pm 0.50	1.25 \pm 0.50	0.79 \pm 0.52	1.27 \pm 0.47	0.78 \pm 0.51
Trial 9	0.165 \pm 0.10	0.484 \pm 0.13	0.860 \pm 0.13	1.827 \pm 0.17	0.84 \pm 0.45	3.39 \pm 0.80	0.84 \pm 0.44	3.44 \pm 0.70
Trial 10	0.164 \pm 0.07	0.666 \pm 0.13	0.982 \pm 0.11	3.119 \pm 0.50	1.21 \pm 0.57	1.44 \pm 1.04	1.25 \pm 0.56	1.49 \pm 1.03
Total	0.211 \pm 0.07	0.630 \pm 0.25	0.956 \pm 0.13	2.623 \pm 0.43	1.226 \pm 0.51	3.61 \pm 0.99	1.23 \pm 0.46	3.71 \pm 0.76

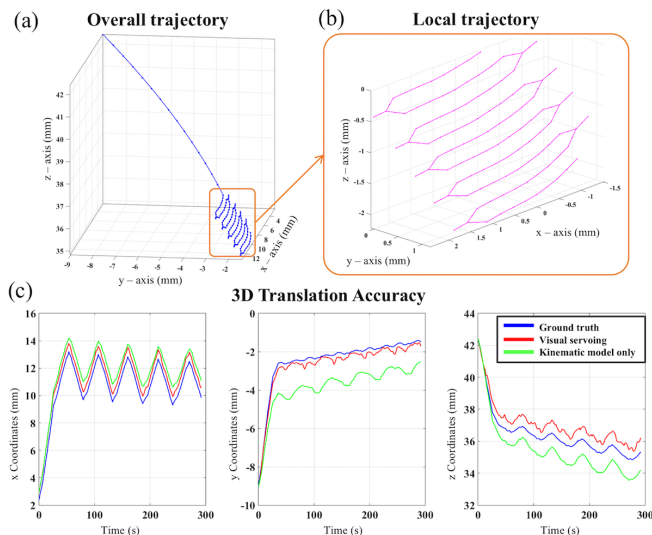


Fig. 4. Exemplar trajectory planning and results over a 2x2 mm tissue surface area for pCLE scanning. (a) Overall planned trajectory (ground truth) from a random starting location; (b) Planned local scanning trajectory of (a); (c) 3D translation accuracies of trial 8, where both trajectories using visual servoing and kinematic-only control are compared to ground truth.

with Visual Servoing (VS) and Kinematic Motion (KM) only. The planned trajectories were used as the ground truth, and both the optical tracked results of two runs were transformed into the camera frame for comparison. Two types of errors were computed, the overall error that assesses both the global and local trajectories, and the local error that assesses only the local trajectories after aligning their starting positions. For both, the measured translational errors and rotational errors are summarised in Table II.

Fig. 4 shows an example of global and local trajectories from trial 8, as well as the 3D translation accuracies of both the visual servoing approach and kinematic-only control. It can be seen from Fig. 4(c) that the trajectories of both approaches start at the same position, however, the trajectory of kinematic-only control deviates from the ground truth as the robot moves. Based on the overall error values from Table II, both translational and rotational accuracies are significantly improved over the accuracies of kinematic-only control. We have also observed that in all of the trials, motion

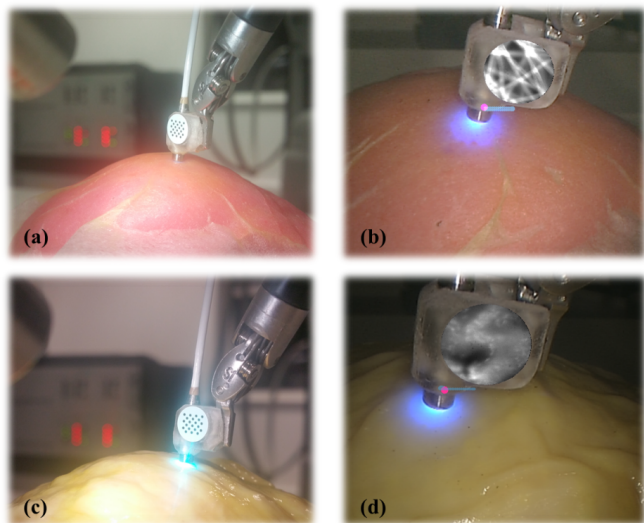


Fig. 5. Snapshots of the phantom and *ex vivo* experiments. (a) and (c) Experimental setups; (b) and (d) A snapshot of the user interface, where the pink dot represents the probe tip location and blue lines indicates planned local trajectory. The KeyDot[®] marker was overlaid with the streaming microscopic images for augmented reality.

with visual servoing was able to achieve sub-millimetre accuracy (3D translation). It is important to note that, for the accuracy of the local trajectory, the motion with visual servoing has achieved 0.211 mm, which is smaller than the FoV (0.24 mm) of the endomicroscope. For orientation errors, both the local and overall results (see Table II) have shown that the visual control approach provides lower errors than the kinematic-only approach.

C. Phantom and Ex Vivo Experiment

In this work, we have performed autonomous scans on a custom-made PVA cryogel kidney phantom. In order to produce high quality microscopic images, lens tissue paper stained with the topical fluorescent contrast agent acriflavine, was placed on top of the surface. A snapshot of the experiment is provided in Fig. 5(a-b). The scanning tasks were then performed on the phantom surface using the raster trajectories. An example of the obtained 2D mosaics is shown in Fig. 6(a), where a 3x3 mm region is covered. The actual covered region is slightly larger than 3x3 mm,

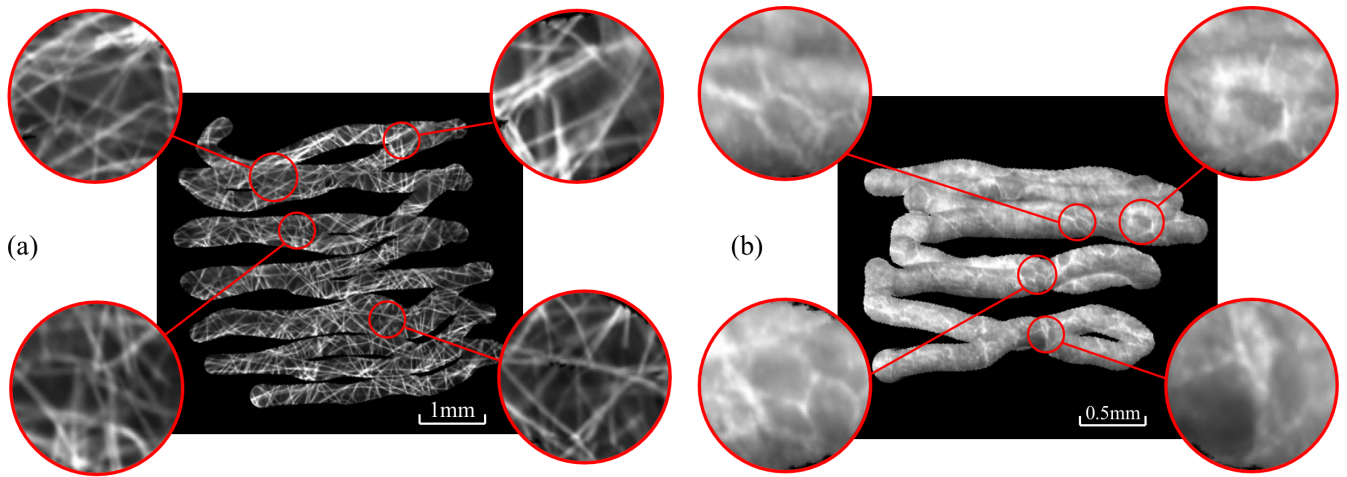


Fig. 6. Exemplar 2D mosaicing results. (a) Mosaics of a 3x3 mm region on a kidney phantom; (b) Mosaics of a 2x2 mm region on an *ex vivo* porcine colon fat tissue sample.

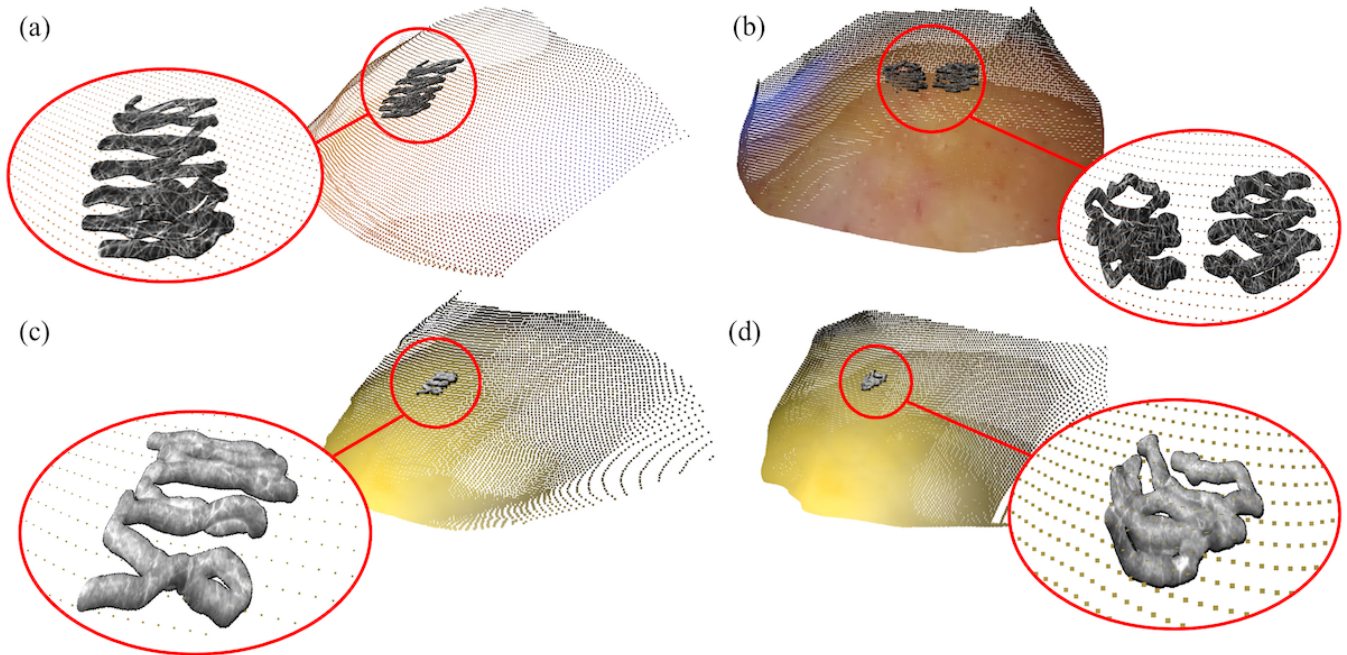


Fig. 7. Exemplar 3D fusion results. (a) Online fusion results and (b) Multi-region fusion results of the phantom experiments; (c) and (d) Online fusion results of the *ex vivo* colon experiment.

due to the extra loading-unloading phase. The 3D fusion results are presented in Fig. 7(a) and (b), where Fig. 7(b) also demonstrates that our approach is able to perform multi-region scanning. These results have shown our proposed framework is able to provide continuous image mosaicing, benefiting from the smooth and accurate motion generated by the visual servoing approach.

Experiments were also performed using *ex vivo* animal tissue (see Fig. 5(c-d)). A porcine colon fat tissue sample was again stained with the topical acriflavine contrast agent. Examples of the 2D mosaicing and 3D fusion results are provided in Fig. 6(b), and Fig. 7(c) and (d), respectively. Both the phantom and *ex vivo* experiments have demonstrated that

our framework is capable of performing autonomous large area 3D scans while generating high quality image mosaics. It is also worth mentioning that due to the advantage of global surface reconstruction and visual servo control, we are able to scan multiple regions on the same surface. To this end, the robot moves the probe to an original standby pose after each scan is completed, and a new scanning region can be selected on the same surface.

D. Discussion

The overall mosaicing results strongly depend on the desired trajectory, planned according to the stereo reconstruction. Whilst one might expect that the accuracy of stereo

reconstruction is insufficient for an endomicroscopy scanning task, we found in the experiments that most of the scanning tasks can be completed successfully. However, it was observed during the stereo validation that the recovered surface tended to have a constant offset despite maintaining good shape compared to the ground truth. To address this error offset, we adjusted the probe tip to marker transformation \mathbf{T}_D^M to ensure the continuous contact with the surface. This solution is not ideal and would cause problem when the reconstruction error becomes too large ($> 2.0mm$). This is because the large error would cause the probe to either lose contact with the surface or apply too much pressure, leading to excessive deformation. In addition, we also observed that the image quality tends to decrease as the contact force increases. A comprehensive solution to this problem, would be to perform additional visual servoing based on the the microscopic images. With this, the image quality could then be used to detect loss of contact or excessive pressure, as well as to adjust the robot position accordingly.

The proposed framework presents good repeatability and accuracy as shown in Table II, where all trials present consistently low errors to allow for the endomicroscopic scanning task. The final mosaicing results of both phantom and *ex vivo* experiments, as shown in Fig. 6, have demonstrated that the system is capable of scanning a large region while obtaining reasonable quality mosaicing results. We should also note that the mosaicked areas are not fully covered due to the fact that a pairwise image registration approach would accumulate errors on 3D non-planar surfaces. To generate a continuous 2D mosaic would require a non-rigid, global mosaic optimisation algorithm that is unlikely to be real time. Nevertheless, the sparse mosaics generated in this work are a significant improvement over the basic linear mosaics produced by manually operated endomicroscopes, which would still have important clinical value for intraoperative pathological analysis and surgical planning.

IV. CONCLUSION AND FUTURE WORK

In this paper, an autonomous framework using the da Vinci[®] robot is proposed for endomicroscopic mosaicing and online fusion of 3D reconstructed macroscopic images with microscopic images. We have implemented a 6-DoF visual servoing approach to achieve continuous and smooth scanning. In addition, the proposed framework provides a comprehensive visualisation to users, which includes: (1) an overlay of microscopic images into the surgical view for augmented reality; (2) an online updating 2D mosaic image; and (3) 3D fusion of the mosaic image with the tissue surface on-the-fly. These visualisation options have a range of potential benefits for intraoperative tissue pathology analysis and surgical planning, which will be explored in future work. The proposed framework has been tested on phantoms and *ex vivo* tissue, and quantitative results obtained from an external tracking system have shown that our framework can achieve accuracy better than the FoV of the endomicroscope, thus permitting smooth and accurate microscopic scanning. Future work will focus on improving

the image mosaic quality via visual servoing on microscopic images. To increase the robustness of the framework in a realistic clinical environment, we will also consider tissue deformations due to respiratory motion and other dynamic events during RMIS procedures.

ACKNOWLEDGMENT

The authors would like to thank Simon DiMaio from Intuitive Surgical Inc for providing the CAD model of the large needle driver, Konrad Leibrandt for his assistance with the software, and Stamatia Giannarou for valuable discussions.

REFERENCES

- [1] G. Moustris, S. Hiridis, K. Deliparaschos, and K. Konstantinidis, "Evolution of autonomous and semi-autonomous robotic surgical systems: a review of the literature," *The International Journal of Medical Robotics and Computer Assisted Surgery*, vol. 7, no. 4, pp. 375–392, 2011.
- [2] S. Billings, N. Deshmukh, H. J. Kang, R. Taylor, and E. M. Boctor, "System for robot-assisted real-time laparoscopic ultrasound elastography," in *SPIE Medical Imaging*. International Society for Optics and Photonics, 2012, pp. 83 161W–83 161W.
- [3] A. Ruzskowski, O. Mohareeri, S. Lichtenstein, R. Cook, and S. Salcudean, "On the feasibility of heart motion compensation on the davinci[®] surgical robot for coronary artery bypass surgery: Implementation and user studies," in *Robotics and Automation (ICRA), 2015 IEEE International Conference on*. IEEE, 2015, pp. 4432–4439.
- [4] N. Padoy and G. D. Hager, "Human-machine collaborative surgery using learned models," in *Robotics and Automation (ICRA), 2011 IEEE International Conference on*. IEEE, 2011, pp. 5285–5292.
- [5] A. Murali, S. Sen, B. Kehoe, A. Garg, S. McFarland, S. Patil, W. D. Boyd, S. Lim, P. Abbeel, and K. Goldberg, "Learning by observation for surgical subtasks: Multilateral cutting of 3d viscoelastic and 2d orthotropic tissue phantoms," in *Robotics and Automation (ICRA), 2015 IEEE International Conference on*, May 2015, pp. 1202–1209.
- [6] P. Pratt, A. Hughes-Hallett, L. Zhang, N. Patel, E. Mayer, A. Darzi, and G.-Z. Yang, "Autonomous ultrasound-guided tissue dissection," in *Medical Image Computing and Computer-Assisted Intervention–MICCAI 2015*. Springer, 2015, pp. 249–257.
- [7] D. Hu, Y. Gong, B. Hannaford, and E. J. Seibel, "Semi-autonomous simulated brain tumor ablation with ravenii surgical robot using behavior tree," in *Robotics and Automation (ICRA), 2015 IEEE International Conference on*. IEEE, 2015, pp. 3868–3875.
- [8] M. B. Wallace, P. Sharma, C. Lightdale, H. Wolfsen, E. Coron, A. Buchner, M. Bajbouj, A. Bansal, A. Rastogi, J. Abrams, *et al.*, "Preliminary accuracy and interobserver agreement for the detection of intraepithelial neoplasia in Barrett's esophagus with probe-based confocal laser endomicroscopy," *Gastrointestinal endoscopy*, vol. 72, no. 1, pp. 19–24, 2010.
- [9] A. Meining, Y. K. Chen, D. Pleskow, P. Stevens, R. J. Shah, R. Chuttani, J. Michalek, and A. Slivka, "Direct visualization of indeterminate pancreaticobiliary strictures with probe-based confocal laser endomicroscopy: a multicenter experience," *Gastrointestinal endoscopy*, vol. 74, no. 5, pp. 961–968, 2011.
- [10] M. Ye, S. Giannarou, N. Patel, J. Teare, and G.-Z. Yang, "Pathological site retargeting under tissue deformation using geometrical association and tracking," in *Medical Image Computing and Computer-Assisted Intervention–MICCAI 2013*. Springer, 2013, pp. 67–74.
- [11] W. T. Latt, R. Newton, M. Visentini-Scarzanella, C. Payne, D. Noonan, J. Shang, and G.-Z. Yang, "A hand-held instrument to maintain steady tissue contact during probe-based confocal laser endomicroscopy," *Biomedical Engineering, IEEE Transactions on*, vol. 58, no. 9, pp. 2694–2703, Sept 2011.
- [12] B. Rosa, M. S. Erden, T. Vercauteren, B. Herman, J. Szwedczyk, and G. Morel, "Building large mosaics of confocal edomicroscopic images using visual servoing," *Biomedical Engineering, IEEE Transactions on*, vol. 60, no. 4, pp. 1041–1049, 2013.
- [13] G. Dwyer, P. Giataganas, P. Pratt, M. Hughes, and G.-Z. Yang, "A miniaturised robotic probe for real-time intraoperative fusion of ultrasound and endomicroscopy," in *Robotics and Automation (ICRA), 2015 IEEE International Conference on*. IEEE, 2015, pp. 1196–1201.

- [14] S. Zuo, M. Hughes, C. Seneci, T. Chang, and G.-Z. Yang, "Towards intraoperative breast endomicroscopy with a novel surface scanning device," *Biomedical Engineering, IEEE Transactions on*, vol. PP, no. 99, pp. 1–1, 2015.
- [15] A. Patsias, L. Giraldez-Rodriguez, A. Polydorides, R. Richards-Kortum, S. Anandasabapathy, T. Quang, A. Sikora, and B. Miles, "Feasibility of transoral robotic-assisted high resolution microendoscopic imaging of oropharyngeal squamous cell carcinoma," *Head & neck*, 2014.
- [16] P. Giataganas, M. Hughes, and G.-Z. Yang, "Force adaptive robotically assisted endomicroscopy for intraoperative tumour identification," *International journal of computer assisted radiology and surgery*, pp. 1–8, 2015.
- [17] P. Giataganas, C. Bergeles, P. Pratt, M. Hughes, A. Darzi, and G.-Z. Yang, "Intraoperative 3d fusion of microscopic and endoscopic images in transanal endoscopic microsurgery," in *The Hamlyn Symposium on Medical Robotics*, 2014, p. 35.
- [18] M. Hughes and G.-Z. Yang, "High speed, line-scanning, fiber bundle fluorescence confocal endomicroscopy for improved mosaicking," *Biomedical optics express*, vol. 6, no. 4, pp. 1241–1252, 2015.
- [19] Z. Zhang, "A flexible new technique for camera calibration," *Pattern Analysis and Machine Intelligence, IEEE Transactions on*, vol. 22, no. 11, pp. 1330–1334, Nov 2000.
- [20] P. Kazanzides, Z. Chen, A. Deguet, G. S. Fischer, R. H. Taylor, and S. P. DiMaio, "An open-source research kit for the da vinci® surgical system," in *Robotics and Automation (ICRA), 2014 IEEE International Conference on*. IEEE, 2014, pp. 6434–6439.
- [21] A. Geiger, M. Roser, and R. Urtasun, "Efficient large-scale stereo matching," in *Computer Vision–ACCV 2010*. Springer, 2011, pp. 25–38.
- [22] M. S. Erden, B. Rosa, J. Szewczyk, and G. Morel, "Understanding soft-tissue behavior for application to microlaparoscopic surface scan," *IEEE Transactions on Biomedical Engineering*, vol. 60, no. 4, pp. 1059–1068, April 2013.
- [23] R. Y. Tsai and R. K. Lenz, "A new technique for fully autonomous and efficient 3d robotics hand/eye calibration," *Robotics and Automation, IEEE Transactions on*, vol. 5, no. 3, pp. 345–358, 1989.
- [24] P. Pratt, A. Di Marco, C. Payne, A. Darzi, and G.-Z. Yang, "Intraoperative ultrasound guidance for transanal endoscopic microsurgery," in *Medical Image Computing and Computer-Assisted Intervention–MICCAI 2012*. Springer, 2012, pp. 463–470.
- [25] J.-Y. Bouguet, "Pyramidal implementation of the affine lucas kanade feature tracker description of the algorithm," *Intel Corporation*, vol. 5, pp. 1–10, 2001.
- [26] V. Lepetit, F. Moreno-Noguer, and P. Fua, "Epnnp: An accurate o (n) solution to the pnp problem," *International journal of computer vision*, vol. 81, no. 2, pp. 155–166, 2009.
- [27] T. Vercauteren, A. Meining, F. Lacombe, and A. Perchant, "Real time autonomous video image registration for endomicroscopy: fighting the compromises," in *Biomedical Optics (BiOS) 2008*. International Society for Optics and Photonics, 2008, pp. 68 610C–68 610C.
- [28] P.-L. Chang, D. Stoyanov, A. J. Davison, *et al.*, "Real-time dense stereo reconstruction using convex optimisation with a cost-volume for image-guided robotic surgery," in *Medical Image Computing and Computer-Assisted Intervention–MICCAI 2013*. Springer, 2013, pp. 42–49.